Structure
Article

Structural Insights into Atg10-Mediated Formation of the Autophagy-Essential Atg12-Atg5 Conjugate

Masaya Yamaguchi,[1] Nobuo N. Noda,[2,*] Hayashi Yamamoto,[3] Takayuki Shima,[3] Hiroyuki Kumeta,[1] Yoshihiro Kobashigawa,[1] Rinji Akada,[4] Yoshinori Ohsumi,[3] and Fuyuhiko Inagaki[1,*]
[1]Department of Structural Biology, Faculty of Advanced Life Science, Hokkaido University, Sapporo 001-0021, Japan
[2]Institute of Microbial Chemistry, Tokyo, Tokyo 141-0021, Japan
[3]Frontier Research Center, Tokyo Institute of Technology, Yokohama 226-8503, Japan
[4]Department of Applied Molecular Bioscience, Yamaguchi University Graduate School of Medicine, Ube 755-8611, Japan
*Correspondence: nn@bikaken.or.jp (N.N.N.), finagaki@pharm.hokudai.ac.jp (F.I.)
DOI 10.1016/j.str.2012.04.018

SUMMARY

The Atg12-Atg5 conjugate, which is formed by an ubiquitin-like conjugation system, is essential to autophagosome formation, a central event in autophagy. Despite its importance, the molecular mechanism of the Atg12-Atg5 conjugate formation has not been elucidated. Here, we report the solution and crystal structures of Atg10 and Atg5 homologs from Kluyveromyces marxianus (Km), a thermotolerant yeast. KmAtg10 comprises an E2-core fold with characteristic accessories, including two β strands, whereas KmAtg5 has two ubiquitin-like domains and a helical domain. The nuclear magnetic resonance experiments, mutational analyses, and cross-linking experiments showed that KmAtg10 directly recognizes KmAtg5, especially its C-terminal ubiquitin-like domain, by its characteristic two β strands. Kinetic analysis suggests that Tyr56 and Asn114 of KmAtg10 may place the side chain of KmAtg5 Lys145 into the optimal orientation for its conjugation reaction with Atg12. These structural features enable Atg10 to mediate the formation of the Atg12-Atg5 conjugate without a specific E3 enzyme.

INTRODUCTION

Autophagy is an intracellular degradation system conserved among eukaryotes from yeasts to mammals. In autophagy, cup-shaped membrane structures called isolation membranes expand and sequester cytoplasmic components and organelles, which seal to become double-membrane-bound structures called autophagosomes (Klionsky and Ohsumi, 1999; Mizushima et al., 2011; Nakatogawa et al., 2009). Autophagosome contents are eventually delivered to vacuoles in yeast or lysosomes in mammals. In higher eukaryotes, autophagy plays a crucial role in fundamental biological processes, such as intracellular clearance, differentiation, development, cell death, and antigen representation, and autophagy dysfunction is associated with disease, such as neurodegenerative disorders and cancers (Mizushima, 2007). The formation step of autophagosomes requires two ubiquitin-like conjugation systems called the Atg8 and the Atg12 system (Noda et al., 2009; Ohsumi, 2001).

Ubiquitin (Ub) and ubiquitin-like proteins (Ubls) are ligated to substrate lysine ε-amino groups in a sequential manner (Hershko and Ciechanover, 1998). Ub/Ubls are first activated by E1 enzymes and then transferred to E2 enzymes to form E2∼Ub/Ubl thioester intermediates (where ∼means a thioester bond). Finally, Ub/Ubls are transferred from E2∼Ub/Ubl thioester to the substrate acceptor lysine, which for the most part requires E3 ligases. In the Atg12 system, the C-terminal glycine (Gly120) of Atg12 (a Ubl) is activated by Atg7 (an E1-like enzyme) to form an Atg7∼Atg12 thioester intermediate and is then transferred to Atg10 (an E2-like enzyme) to form an Atg10∼Atg12 thioester intermediate. Atg12 is finally conjugated to the Lys149 side chain of Atg5 via an isopeptide linkage (Mizushima et al., 1998; Shintani et al., 1999; Tanida et al., 1999). Atg5 is a 294 amino acid protein that forms a stable complex with Atg16, a coiled-coil protein, both of which have little sequence homology with functionally characterized proteins (Mizushima et al., 1998, 1999). In the Atg8 system, Atg8 (a Ubl) is conjugated to the amino group of a phosphatidylethanolamine (PE) via the reactions catalyzed by Atg7 and Atg3 (an E2-like enzyme) (Ichimura et al., 2000). In vitro and in vivo studies have shown that the Atg12-Atg5 conjugate promotes conjugation between Atg8 and PE, which is achieved through direct interaction with Atg3 (Fujioka et al., 2008; Fujita et al., 2008; Hanada et al., 2007; Suzuki et al., 2001).

Atg10 achieves Atg12-Atg5 conjugation in an E3-enzyme independent manner; however, the molecular details of how Atg10 mediates the transfer of Atg12 to Atg5 remain unclear. Although the structure of Atg5-Atg16 complex has revealed the unique domain architecture of Atg5 comprising two ubiquitin-like domains and a helical domain (Matsushita et al., 2007), it remains to be elucidated whether the unique architecture is conserved among Atg5 homologs and whether Atg16-binding has some influences on that. Furthermore, the molecular role of each Atg5 domain has not been established. To address these issues, structural and functional analyses of Atg10 and Atg5 using their homologs from a thermotolerant yeast, *Kluyveromyces marxianus* (KmAtg proteins) (Nonklang et al., 2008), were performed. Taking advantage of the higher stability of KmAtg proteins (H.Y. and Y.O., unpublished data), two structures, the solution structure of KmAtg10 and the crystal structure of KmAtg5, were obtained. The KmAtg10-KmAtg5

Table 1. Structural Statistics of KmAtg10	
NOE distance constraints	3,282
Short range (intraresidue and sequential)	1,805
Medium range ($2 \leq \|i-j\| \leq 4$)	520
Long range ($\|i-j\| > 4$)	957
TALOS angle constraints (φ and ψ)	225
Number of violations	
Distance > 0.2 Å	4
Angles > 3°	1
Structural coordinates rmsd (Å) (range 4–141)	
Backbone atoms	0.53
All heavy atoms	0.95
Ramachandran plot	
Most-favored regions (%)	77.9
Additionally allowed regions (%)	21.6
Generously allowed regions (%)	0.5
Disallowed regions (%)	0.0

interaction was then characterized by nuclear magnetic resonance (NMR) experiments and biochemical assays, which established the structural basis of the Atg10-mediated formation of the Atg12-Atg5 conjugate and explained how the E2 enzyme mediates the conjugation reaction without a specific E3 enzyme.

RESULTS

KmAtg10 Has an E2-Core Fold with Characteristic Accessories

We previously reported on the crystallization of *Saccharomyces cerevisiae* (Sc) Atg10 (Yamaguti et al., 2007), but trials to determine its structure were unsuccessful because of crystal twinning problems. ScAtg10 has an aggregate-prone nature that is also not suited to NMR study (H.Y. and Y.O., unpublished data). In general, proteins in thermophile organisms show higher stability compared with their homologous proteins in nonthermophile organisms. *K. marxianus* (Km), a thermotolerant yeast that is closely related to *Saccharomyces cerevisiae*, possesses homologous genes for all the Atg proteins constituting Atg8 and Atg12 systems, suggesting that they are also conserved in this yeast. With the expectation of higher stability, we selected KmAtg10 for structural study and succeeded in determining the solution structure of KmAtg10 by NMR spectroscopy. Assignments of the ^{1}H-^{15}N HSQC spectrum (Biological Magnetic Resource Bank ID: 18277) and the overlay of the 20 structures of KmAtg10 are shown in Figures S1A and S1B (available online), respectively, and structural statistics are shown in Table 1. Ribbon diagram of the lowest energy structure of KmAtg10 is shown in Figure 1A, left. The overall structure of KmAtg10 comprises four α helices (A-D) and seven β strands (1-6 and 4′).

For comparison, the structure of Ubc9, an E2 enzyme for small ubiquitin-like modifier (SUMO) that possesses a canonical E2 fold is shown in Figure 1A, right, in the same orientation. All E2 enzymes reported to date have a conserved E2 core structure composed of a central four-stranded β sheet and two α helices

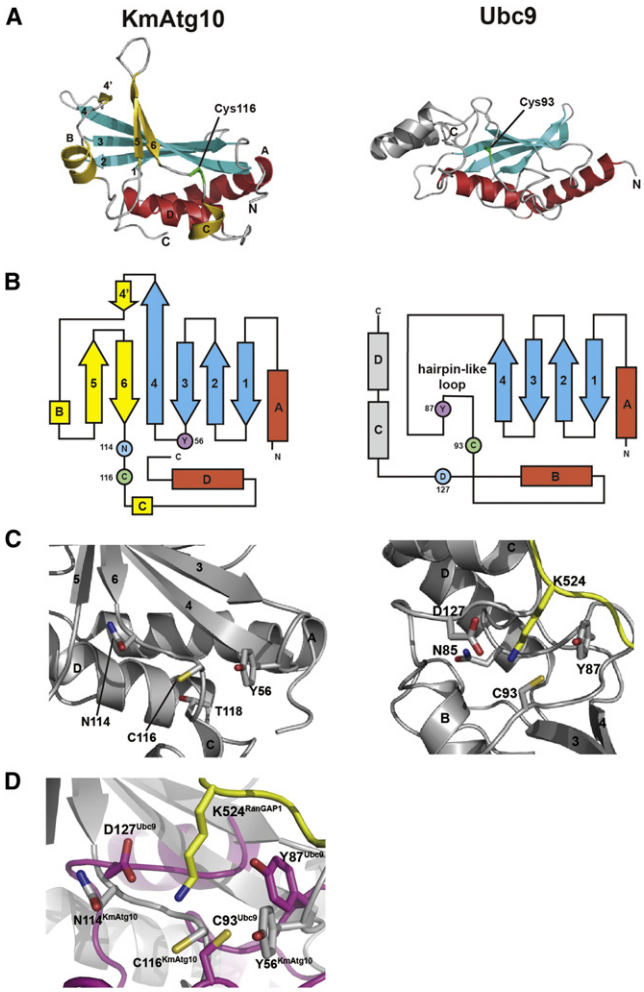

Figure 1. Structure of KmAtg10 and Its Comparison with the Ubc9 Structure

(A) Ribbon diagrams of KmAtg10 (left) and Ubc9 (right) are shown in the same orientation. α helices and β strands included in the E2 core structure are colored red and cyan, respectively, and secondary structures unique to KmAtg10 are colored yellow, whereas secondary structures that are observed in Ubc9 but not in KmAtg10 and loops are colored gray. Four α helices and seven β strands are denoted A-D and 1-6 and 4′, respectively. Amino and carboxyl termini are denoted N and C, respectively. The side chain of the catalytic cysteine of KmAtg10 and Ubc9 is shown with a green stick model.

(B) Topologies of KmAtg10 (left) and Ubc9 (right). Coloring is as in (A). Catalytic cysteines are shown with a circled C and KmAtg10 Tyr56 and Ubc9 Tyr87 are shown with a circled Y, respectively. KmAtg10 Asn114 and Ubc9 Asp127 are shown with a circled N and D, respectively.

(C) Catalytic structure of KmAtg10 (left) and Ubc9 in complex with RanGAP1 (right). Catalytic cysteines and their surrounding important residues are shown with stick models and colored yellow, red, and blue for sulfur, oxygen, and nitrogen atoms, respectively. RanGAP1 is colored yellow.

(D) Superimposition of the catalytic-site structures of KmAtg10 and Ubc9 bound to RanGAP1. Superimposition was performed as described in the Experimental Procedures. Carbon atoms of KmAtg10, Ubc9, and RanGAP1 are colored gray, magenta, and yellow, respectively, whereas other atoms are colored as in (C).

See also Figure S1.

(Figures 1A and 1B). KmAtg10 has the corresponding four-stranded β sheet (β strands 1-4) and two α helices (A, D). Canonical E2 enzymes, including Ubc9, have accessory region(s) at the N terminus and/or the C terminus, which are important for the interaction with binding partners (Wenzel et al., 2011); however, KmAtg10 lacks these at both termini (Figures 1A and 1B). Unlike Ubc9, KmAtg10 has additional two α helices (B, C) and three β strands (4′, 5, 6) inserted in the E2 core (Figures 1A and 1B). Canonical E2s conserve three catalytically important residues in addition to the catalytic cysteine; these are Asn85, Tyr87, and Asp127 in the case of Ubc9. Asn85 constitutes an oxyanion hole and stabilizes a tetrahedral oxyanion intermediate during catalysis (Wu et al., 2003; Yunus and Lima, 2006). However, structural analysis of Ubc9 in complex with its substrate RanGAP1 revealed that the side chains of Tyr87 and Asp127 sandwich and fix the side chain of the acceptor lysine (RanGAP1 Lys524) to the optimal position for the conjugation reaction (Figure 1C, right) (Yunus and Lima, 2006). These mechanisms are believed to be conserved among E2s.

In the case of Atg10, these three residues are not conserved in topologically equivalent positions. However, Tyr56 and Asn114 of KmAtg10 are positioned near the catalytic Cys116, and the spatial relative arrangement of Tyr56, Asn114, and Cys116 of KmAtg10 is quite similar to that of Tyr87, Asp127, and Cys93 of Ubc9 (Figures 1C and 1D). Tyr56 is strictly conserved, whereas Ans114 is type-conserved (Asn or His) among Atg10 homologs (Figures S1F and S1G). As for the Asn85 of Ubc9, its equivalent residue is not observed in the neighborhood of KmAtg10 Cys116. In summary, the structure of Atg10 comprises the E2 core shared with canonical E2s and noncanonical accessories, and the catalytic-site structure is partially similar to that of canonical E2s.

KmAtg10 Directly Interacts with KmAtg5 using β5 and β6

The fact that Atg10 transfers Atg12 to Atg5 without the help of other proteins, such as E3, raises the possibility that Atg10 itself recognizes Atg5. However, there is no evidence for the direct binding of Atg10 and Atg5. Using purified recombinant proteins, we carried out an in vitro pulldown assay and detected weak interaction between Atg5 and Atg10 (Figure S2A). In order to know the Atg10-Atg5 interaction in detail, we used NMR spectroscopy to study the interaction.

We first performed a titration experiment using ^{15}N-labeled KmAtg10 and nonlabeled KmAtg5. When nonlabeled KmAtg5 was titrated into the solution containing ^{15}N-labeled KmAtg10, a number of cross-peaks in the HSQC spectrum of KmAtg10, including Tyr56, Ser85, Val98, Thr99, Leu100, Met104, and Ser108, shifted. Residues with appreciably large chemical shift perturbations are plotted on the structure of KmAtg10 (Figures 2A–2C and S2B). The results showed that the residues with large chemical shift perturbations were clustered at one side of KmAtg10, including β strands 5 and 6 and Tyr56, a strictly conserved residue near Cys116. To further confirm the binding interface of KmAtg10 with KmAtg5, a transferred cross-saturation experiment suitable for determining the contact residues of a weak protein-protein complex of large molecular weight, was performed using ^{2}H, ^{15}N-labeled KmAtg10 and nonlabeled KmAtg5 (Nakanishi et al., 2002). The signal intensity ratio was calculated based on the spectra with and without irradiation. The results showed that the intensities of the residues on β5, β6, and those near the catalytic Cys116, including Arg64, Thr99, Leu100, Val109, Asn114, and Thr118, significantly decreased (Figures 2D–2F and S2D). The cross-peaks of Tyr56 and Tyr110 were attenuated in the course of titration by KmAtg5, suggesting that these residues are likely to be involved in the interaction between KmAtg10 and KmAtg5. Almost all affected residues on the transferred cross-saturation experiment are clustered on one side of Atg10, including Cys116 (Figures 2E and 2F). Among these affected residues, those on β5 and β6 and Tyr56 are also affected on the titration experiments, suggesting that they are particularly important in the interaction with KmAtg5.

In Vitro Reconstitution of the Atg12 Conjugation System for Biochemical Study

In order to investigate the role of each KmAtg10 residue in the conjugation reaction, we next reconstituted the Atg12 conjugation system in vitro using recombinant KmAtg proteins. Although we successfully purified recombinant proteins for KmAtg5, KmAtg7, and KmAtg10, we failed to obtain recombinant KmAtg12 because of its aggregate-prone nature. Among the Atg12 homologs, only the *Arabidopsis thaliana* homolog (AtAtg12b) could be obtained as a soluble protein (Suzuki et al., 2005). Therefore, AtAtg12b was used instead of KmAtg12 for in vitro reconstitution. Purified KmAtg7, KmAtg10, and KmAtg5 with a 6xHis-tag and AtAtg12b were mixed with ATP and incubated for 2 hr at 303 K. A new band at around 40 kDa was detected by both anti-AtAtg12b and anti-6xHis antibodies and was observed only when all constituents of the Atg12 conjugation system were included, indicating that the new band corresponds to the AtAtg12b-KmAtg5 conjugate (calculated molecular weight, 42 kDa) (Figures 3A and 3B).

Using the established reconstitution system, the catalytic cysteine residues of KmAtg7 and KmAtg10, as well as the acceptor lysine of KmAtg5, were studied. Based on the sequence comparison with ScAtg proteins, KmAtg7 C488A, KmAtg10 C116A, and KmAtg5 K145A mutants were prepared and used in conjugation assays, which revealed that all of them were defective in the formation of the AtAtg12b-KmAtg5 conjugate (Figure 3C). Moreover, the KmAtg10∼AtAtg12b thioester intermediate was normally formed when wild-type KmAtg10 but not KmAtg10 C116A was used (Figure 3D). These results clearly showed that KmAtg7 Cys488, KmAtg10 Cys116, and KmAtg5 Lys145 are the catalytic cysteines and the acceptor lysine, respectively, and demonstrated that the reconstituted Atg12 system is useful for functional analysis.

Functional Characterization of the Atg10 Residues Involved in Atg5 Binding

Among the residues affected by NMR experiments, we chose six residues, Tyr56, Arg64, Thr99, Tyr110, Asn114, and Thr118 and prepared KmAtg10 mutants with alanine substitutions. Arg64, Thr99, and Tyr110 are located at β4, β5, and β6, respectively, and expose their side chain, whereas Tyr56, Asn114, and Thr118 are located at loop regions surrounding Cys116. In addition to these six mutants, the Y56F mutant was prepared to study the role of the hydroxyl group of Tyr56. These seven

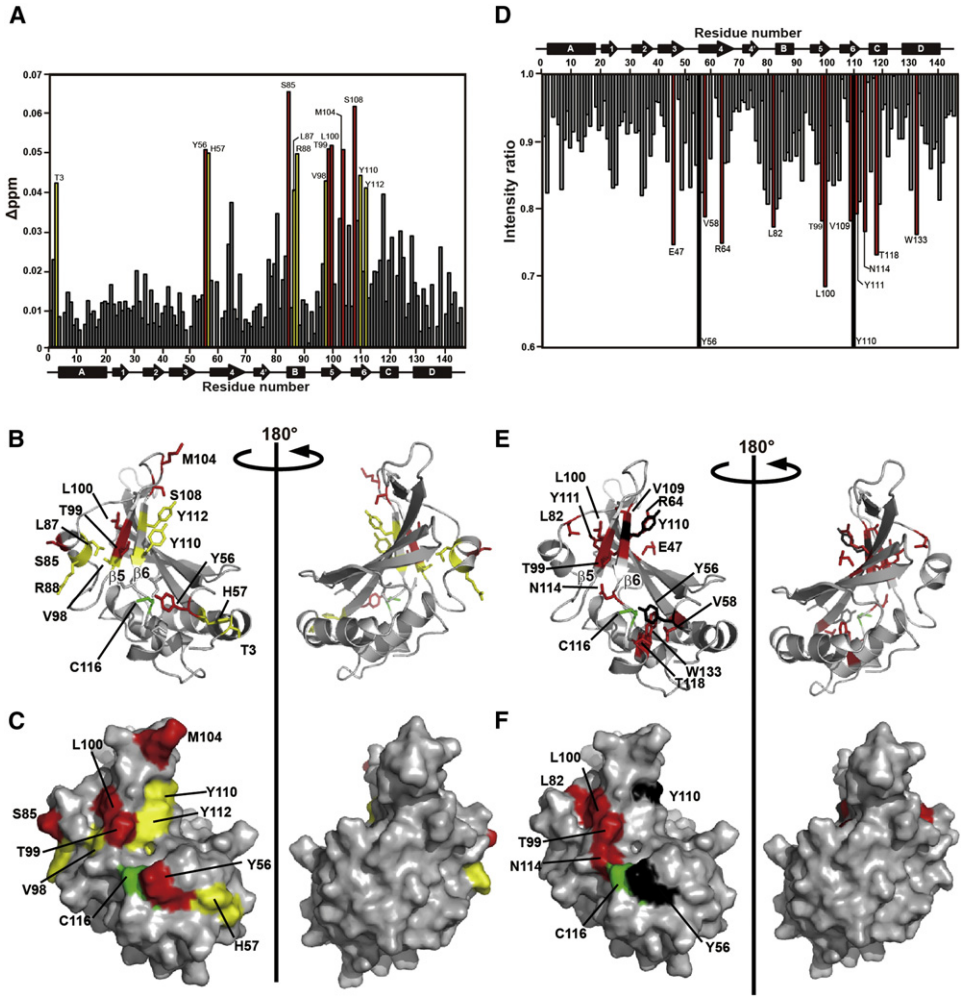

Figure 2. KmAtg10-KmAtg5 Interaction Analyses by NMR

(A) Chemical shift perturbation experiments between KmAtg10 and KmAtg5. The residues with high Δppm values are colored red (>0.05) and yellow (>0.04), respectively. The overlaid six HSQC spectra are shown in Figure S2B.

(B) The residues with high Δppm values are mapped on the structure of KmAtg10 shown in a ribbon diagram, and their side chains are shown with stick models. Coloring is as in (A). The side chain of Cys116 is shown with a green stick model.

(C) Surface representation of B.

(D) Plot of the intensity ratios of the cross-peaks in the transferred cross-saturation experiments. The residues with low intensity ratio are shown with stick models and colored red (<0.8). The ratios for Tyr56 and Tyr110 were not available.

(E) The residues with low intensity ratio are mapped on the ribbon diagram of KmAtg10 (colored red). Tyr56 and Tyr110 are colored black and Cys116 is shown with a green stick model.

(F) Surface representation of (E).

See also Figure S2.

KmAtg10 mutants and C116A were first subjected to in vitro conjugation reactions under multiturnover conditions, and those showing reduced activity were then subjected to in vitro reactions dissected into two steps: the first being the formation of the AtAtg12b∼KmAtg10 thioester intermediate and the second the final transfer of AtAtg12b from KmAtg10 to KmAtg5. For the final transfer reaction, apparent K_m and k_{cat} values were calculated based on kinetic data.

Among the mutants at β4-β6, T99A (β5) and Y110A (β6) mutants showed significantly and slightly reduced levels of the AtAtg12b-KmAtg5 conjugate, respectively, whereas the R64A mutant (β4) showed similar activity to wild-type KmAtg10 (Figures 4A and 4B). The T99A mutant retained normal activity for forming the AtAtg12b∼KmAtg10 intermediate (Figures 4C and 4D) but showed a severe defect in the final transfer step (Figure 4E and 4F). Kinetic analysis revealed that T99A mutation showed a significantly increased K_m value (i.e., weakened affinity) but did not affect the k_{cat} value in the final transfer reaction (Figure 4G). HSQC spectra showed that the effects of the T99A mutation on the protein structure were restricted to microenvironmental changes (Figure S3B). Taken together, these results suggested that KmAtg10 β5 contributes to the

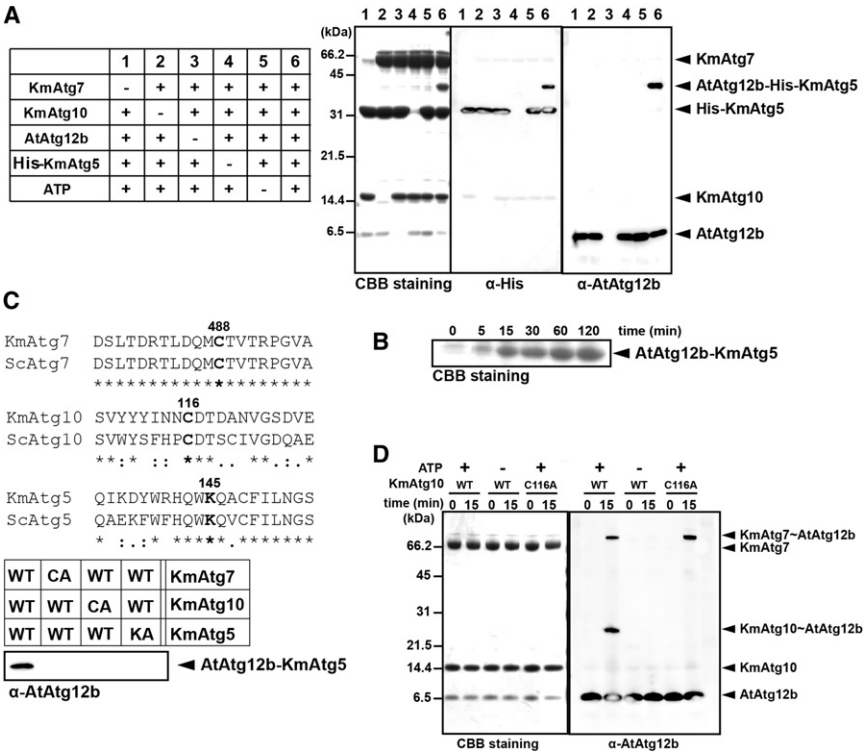

Figure 3. In Vitro Reconstitution of AtAtg12b-KmAtg5 Conjugation System

(A) Where indicated (+) in the table, 10 μM KmAtg7, 10 μM KmAtg10, 10 μM AtAtg12b, and 10 μM His-KmAtg5 were mixed with or without 1 mM ATP (+ or − ATP) and incubated for 2 hr at 303 K. Samples were subjected to SDS-PAGE, and protein bands were detected by CBB staining (left), immunoblotting using anti-6xHis antibodies (middle), or immunoblotting using anti-AtAtg12b antibodies (right).

(B) 10 μM KmAtg7, 10 μM KmAtg10, 10 μM AtAtg12b, and 10 μM KmAtg5 with 1 mM ATP were incubated for the indicated time at 303 K. The sample was subjected to SDS-PAGE, and the AtAtg12b-KmAtg5 band was detected by CBB staining.

(C) (Upper lane) The sequence alignment of the region containing the catalytic cysteine between KmAtg7 and ScAtg7, between KmAtg10 and ScAtg10, and the region containing the acceptor lysine between KmAtg5 and ScAtg5 are shown. The catalytic cysteine of ScAtg7 (Cys507) and ScAtg10 (Cys133) and their equivalent residue of KmAtg7 (Cys488) and KmAtg10 (Cys116) are bold. The acceptor lysine of ScAtg5 (Lys149) and its equivalent residue of KmAtg5 (Lys145) are also bold. (Lower lane) Samples containing 10 μM KmAtg7, 10 μM KmAtg10, 10 μM AtAtg12b, and 10 μM KmAtg5 with 1 mM ATP were incubated for 2 hr at 303 K, and the samples were subjected to SDS-PAGE, followed by immunoblotting using anti-AtAtg12b antibodies. CA in the lanes of KmAtg7 and KmAtg10 indicates C488A and C116A mutants, respectively, whereas KA indicates the K145A mutant of KmAtg5. WT indicates wild-type proteins.

(D) Samples containing 10 μM KmAtg7, 10 μM KmAtg10, and 10 μM AtAtg12b with or without 1 mM ATP were incubated for 15 min at 303 K. The sample was subjected to SDS-PAGE, and the bands for the KmAtg10∼AtAtg12b thioester intermediate and the KmAtg7∼AtAtg12b thioester intermediate were detected by immunoblotting using anti-AtAtg12b antibodies.

affinity with KmAtg5 and that its contribution to the catalysis is low.

All alanine mutants at the loops near Cys116, namely, Y56A, N114A, and T118A, showed significantly reduced levels of the AtAtg12b-KmAtg5 conjugate (Figures 4A and 4B). KmAtg10 Y56F showed normal activity, suggesting that the aromatic ring but not the hydroxyl group of Tyr56 plays an important role in the formation of the AtAtg12b-KmAtg5 conjugate. Y56A, N114A, and T118A all retained normal activity for forming the AtAtg12b∼KmAtg10 intermediate (Figures 4C and 4D), while showing a severe defect in the final transfer step (Figures 4E and 4F). Kinetic analysis revealed that these three mutations showed severely reduced k_{cat} values, whereas their effect on the K_m value is small in the final transfer reaction (Figure 4G). HSQC spectra showed that the effects of Y56A and N114A mutations on the protein structure were restricted to microenvironmental changes (Figures S3A and S3C). On the other hand, a number of residues with large chemical shift perturbations were observed in the T118A mutant, suggesting that Thr118 is important for the proper folding of KmAtg10 and that its mutation induced a conformational change in the wide region of KmAtg10 (Figure S3D). Taken together, these results suggested that Tyr56 and Asn114 play a critical role in catalysis but that their contribution to the affinity with KmAtg5 is restricted, whereas Thr118 contributes to the proper folding of the catalytic site.

To examine in vivo significance of the residues, the formation levels of the Atg12-Atg5 conjugate in *atg10*Δ cells expressing ScAtg10 mutants corresponding to the KmAtg10 mutants shown above were studied. The Atg12-Atg5 conjugation levels in *atg10*Δ cells expressing ScAtg10 Y73A (corresponding to KmAtg10 Y56A), G115F and G115W (KmAtg10 T99A) and H131A (KmAtg10 N114A) decreased compared with those in *atg10*Δ cells expressing wild-type ScAtg10 (Figures S3E and S3F). All these in vivo results of ScAtg10 are consistent with the in vitro results of KmAtg10. Although KmAtg10 Thr99, which is located on β5, is not conserved in ScAtg10 (Figure S1F), the Atg12-Atg5 conjugation levels decreased when using the corresponding residue mutants, G115F and G115W, suggesting that Atg10 β5 is important for the recognition of Atg5 in vivo as well as in vitro.

The K_m value between KmAtg10∼AtAtg12b and KmAtg5 calculated from biochemical analyses was ∼10 μM (Figure 4G), whereas the K_d value between KmAtg10 and KmAtg5 estimated from NMR titration experiments was larger than 1 mM (Figure S2C). These observations suggest that the thioester formation with Atg12 enhances the affinity of Atg10 with Atg5. Although we could not analyze the interaction between KmAtg10∼AtAtg12b and KmAtg5 because of the instability of the thioester intermediate, we could detect the direct interaction between GST-KmAtg5 and AtAtg12b by in vitro pulldown assay (Figure 4H, lane 5). This interaction was not perturbed by

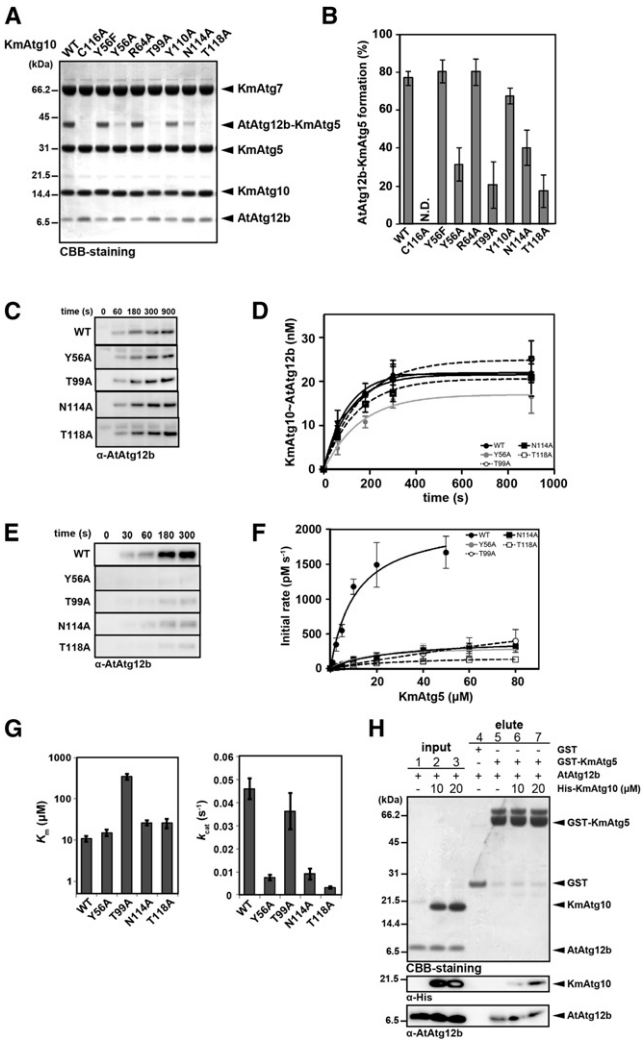

Figure 4. Biochemical Assays Using KmAtg10 Mutants

(A) AtAtg12b-KmAtg5 conjugate formation under multiturnover conditions.

(B) AtAtg12b-KmAtg5 and AtAtg12b bands in (A) were quantified, and the AtAtg12b-KmAtg5 conjugation formation (%) was calculated by dividing the AtAtg12b-KmAtg5 amount by the total AtAtg12b amount. N.D. means not detected.

(C) KmAtg10~AtAtg12b thioester intermediate formation under single-turnover conditions. After generating the KmAtg7~AtAtg12b thioester intermediate, 20 μM KmAtg10 mutants were added. The KmAtg10~AtAtg12b intermediate was detected by immunoblotting using anti-AtAtg12b antibodies.

(D) The amount of the KmAtg10~AtAtg12b thioester intermediate in (C) was quantified and depicted graphically.

(E) AtAtg12b-KmAtg5 conjugate formation under single-turnover conditions. After generating the KmAtg10~AtAtg12b thioester intermediate, 10 μM KmAtg5 was added. The AtAtg12b-KmAtg5 conjugate was detected by immunoblotting using anti-AtAtg12b antibodies.

(F) Initial rates of AtAtg12b-KmAtg5 formation are plotted.

(G) K_m (left) and k_{cat} (right) for AtAtg12b-KmAtg5 formation are depicted graphically.

(H) In vitro pulldown assay between GST-KmAtg5 and AtAtg12b. (Upper) Shows the Coomassie Brilliant Blue staining of the gel. (Middle and bottom) Detect the bands of His-KmAtg10 and AtAtg12b using anti-6xHis and anti-AtAtg12b antibodies, respectively. All biochemical assays were performed in triplicate. Values and error bars represent means and standard deviations, respectively.

See also Figure S3.

KmAtg10 (Figure 4H, lane 6, 7), suggesting that the binding sites on KmAtg5 for AtAtg12b and KmAtg10 do not overlap with each other. These results suggested that KmAtg10~AtAtg12b possesses higher affinity against KmAtg5 than free KmAtg10 by the summation of KmAtg10-KmAtg5 and AtAtg12b-KmAtg5 interactions.

KmAtg5 UblB Interacts with KmAtg10 Using β7

To obtain structural information on KmAtg5, we next determined its crystal structure at a resolution of 2.5 Å (Figure 5A; Table 2). The structure of KmAtg5 comprises nine α helices (A-I) and 10 β strands (1-10), which fold into three domains: the N-terminal ubiquitin-like domain (UblA), the helix-rich domain (HR), and the C-terminal ubiquitin-like domain (UblB). These three domains, with the help of the additional N-terminal helix, gather to form a globular fold. Although this is the first structural report of Atg5 homologs as a free form, we previously reported the crystal structure of ScAtg5 as a complex with the N-terminal region of Atg16 (Matsushita et al., 2007). The KmAtg5 structure, including the topology and domain organization, is quite similar to that of ScAtg5. KmAtg5 Lys145 and ScAtg5 Lys149, the conjugation sites for Atg12, are also well superimposed. These results also suggest that Atg16-binding does not cause a large conformational change in Atg5.

We next examined which region of Atg5 is necessary for the interaction with Atg10. NMR experiments and in vitro mutational assays identified the important residues of KmAtg10 for the interaction with KmAtg5. Because these residues are located within ~20 Å from the catalytic cysteine, Cys116, it raised the possibility that the KmAtg5 residues crucial for the interaction with KmAtg10 are also located within ~20 Å from the acceptor lysine, Lys145. In addition to the distance restraint, the sequence conservation and the surface exposure were used as criteria to prepare KmAtg5 mutants (Figures S4A–S4C). These KmAtg5 mutants were used for in vitro conjugation assays. The AtAtg12b-KmAtg5 conjugation levels using L127A, V208A, and Q210A mutants of KmAtg5, especially the Q210A mutant, decreased compared with that using wild-type KmAtg5 (Figures 5B and 5C). Both Val208 and Gln210 are located on β7 of KmAtg5 UblB.

To further characterize the Atg10-Atg5 interaction, we performed site-specific crosslinking experiments using a sulfhydryl-to-sulfhydryl crosslinker. To interpret the results more readily, the C116A mutation was introduced to all mutants used for the following experiments. We introduced a cysteine substitution at Thr99 on β5 and at Tyr110 on β6 of KmAtg10 and at Val208 and Gln210 on KmAtg5 β7. When either KmAtg10 T99C or Y110C was mixed with KmAtg5 V208C or Q210C and $BM(PEG)_2$, a sulfhydryl-to-sulfhydryl crosslinker, the crosslinking product was clearly detected only for the pair between KmAtg10 T99C and KmAtg5 Q210C near 45 kDa (Figure 5D). This crosslinking product could be detected only in the case in which all constituents were included (Figure S4D), suggesting that it is the KmAtg10-KmAtg5 complex (calculated molecular weight, 48 kDa). Because KmAtg10 Thr99 is located at the β5, additional mutants at the same strand (KmAtg10 S97C, S101C, and D103C) were prepared and used for crosslinking experiments with three KmAtg5 mutants (L127C, V208C, and Q210C) (Figures 5E and S4E), which showed that all

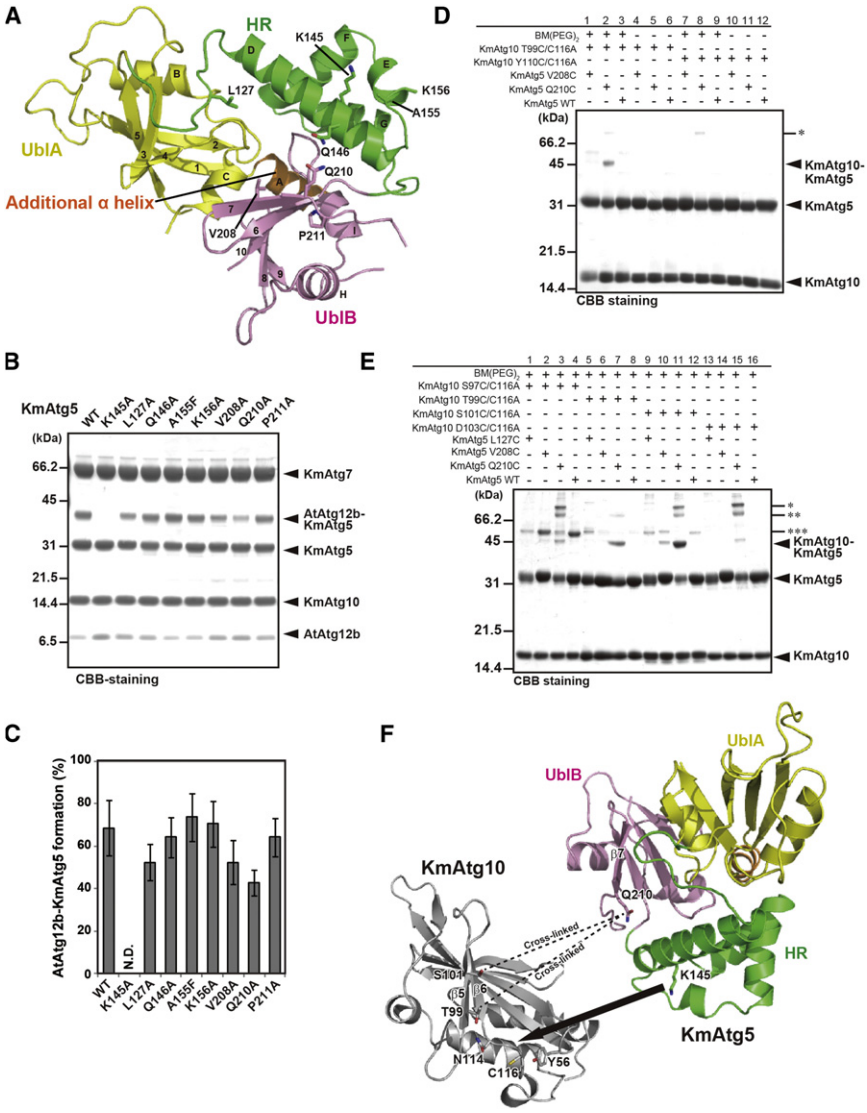

Figure 5. Biochemical Assays based on the Crystal Structure of KmAtg5

(A) The overall structure of KmAtg5 is shown. The additional helix, UblA, HR, and UblB are colored orange, yellow, green, and pink, respectively. Nine α helices and ten β strands are denoted A-I and 1-10, respectively. The side chains of Leu127, Lys145, Gln146, Ala155, Lys156, Val208, Gln210, and Pro211 are shown with stick models. The side chain of Lys156 is poorly defined in the electron density map, so only Cβ is shown.

(B) AtAtg12b-KmAtg5 conjugate formation under multiturnover conditions.

(C) AtAtg12b-KmAtg5 and AtAtg12b bands in (B) were quantified and the AtAtg12b-KmAtg5 conjugation formation (%) was calculated by dividing the AtAtg12b-KmAtg5 amount by the total AtAtg12b amount. N.D. means not detected. Assays were performed in triplicate. Values and error bars represent means and standard deviations, respectively.

(D) Initial crosslinking experiments. Where indicated (+) in the table, 10 μM indicated KmAtg10 and 10 μM indicated KmAtg5 were mixed with (+) or without (-) 100 μM $BM(PEG)_2$ and incubated for 1 hr at room temperature. * indicates unexpected KmAtg5 crosslinked products.

(E) More detailed crosslinking experiments. Where indicated (+) in the table, 10 μM KmAtg10 and 10 μM KmAtg5 were mixed with (+) 100 μM $BM(PEG)_2$ and incubated for 1 hr at room temperature. * and ** indicate unexpected KmAtg5 crosslinked products. *** indicates unexpected KmAtg10-KmAtg5 crosslinked products.

(F) Summary of KmAtg10-KmAtg5 interactions. KmAtg10 β5 and KmAtg5 β7 directly interact with each other, possibly through forming an intermolecular β sheet (crosslinked residues are connected with a broken line). KmAtg5 K145 accesses the catalytic cysteine (Cys116) of KmAtg10 through the interval between the side chains of Tyr56 and Asn114 (black arrow).

See also Figure S4.

KmAtg10 mutants, especially S101C, were crosslinked with KmAtg5 Q210C. The S101C mutant was also crosslinked with KmAtg5 V208C with low efficiency but not with KmAtg5 L127C. Taken together, these results showed that KmAtg10 directly recognizes the second β strand of KmAtg5 UblB (β7) using β5.

DISCUSSION

Here, we determined the solution structure of Atg10 using a thermotolerant yeast homolog, KmAtg10, and showed that Atg10 has an E2-core fold with noncanonical, characteristic accessories. NMR and biochemical analyses demonstrated that Atg10 directly interacts with Atg5 using β5 and β6, the characteristic accessories, and revealed the critical residues of Atg10 for catalysis. Further, we also determined the crystal structure of KmAtg5 and performed structure-based biochemical analyses, which clearly demonstrated that KmAtg5 β7 is involved in the interaction with KmAtg10 β5. Figure 5F summarizes the proposed interactions between KmAtg10 and KmAtg5.

We previously showed that the Atg5 structure contains two Ubls, UblA and UblB; however, the functions of these two Ubls have remained to be elucidated. In this paper, we demonstrated that UblB is responsible for the interaction with Atg10 using the second β strand (β7). The second β strand of UblB is topologically equivalent to β2 of Atg8. It has been reported that Atg8-family proteins utilize their β2 to interact with the Atg8-family-interacting motif (AIM) in other molecules through forming an intermolecular β sheet and function in selective autophagy (Noda et al., 2008, 2010; Yamaguchi et al., 2010). Similarly, it is possible that KmAtg5 UblB interacts with KmAtg10 by forming an intermolecular β sheet between KmAtg5 β7 and KmAtg10 β5. To confirm this hypothesis and to uncover the detailed interaction between Atg10 and Atg5, further structural approaches, such as a cocrystallization trial, are needed.

Despite the low sequence similarity between KmAtg10 and Ubc9, the relative spatial positions of Tyr56 and Asn114 to

Table 2. Data Collection and Refinement Statistics

Data Collection	
Space group	C2
Beamline	Spring8 BL41XU
Cell dimensions	
a, b, c (Å)	165.7, 81.9, 158.5
α, β, γ (°)	90.0, 92.393, 90.0
Wavelength (Å)	1.000
Resolution range (Å)	50.0–2.40 (2.44–2.40)
Observed reflections	370,566
Unique reflections	83,071
Redundancy	4.5 (2.3)
Completeness (%)	97.9 (99.3)
R merge (I)	0.056 (0.440)
Refinement statistics	
Resolution range (Å)	35.15–2.50
Reflection used	69,845
No. of proteins atoms	9,852
No. of heterogen atoms	120
No. of water atoms	77
R_{work}/R_{free}	0.238/0.268
Rmsd from ideality	
Bond length (Å)	0.008
Bond angles (°)	1.4

Values in parentheses refer to the outer shell.

Cys116 in KmAtg10 are quite similar to those of Tyr87 and Asp127 to Cys93 in Ubc9 (Figures 1C and 1D). Asn85, Tyr87, and Asp127 of Ubc9 are responsible for orienting the side chain of the acceptor lysine (Lys524) of RanGAP1. Biochemical assays have shown that these residues are responsible for catalysis but not for binding RanGAP1 (Yunus and Lima, 2006). Our biochemical assays showed that KmAtg10 Tyr56 and Asn114 contribute to catalysis rather than the affinity with KmAtg5. These facts suggested that Tyr56 and Asn114 function as a platform for orienting the acceptor lysine (Lys145) of KmAtg5 in a similar manner with Tyr87 and Asp127 of Ubc9, although their topological locations are quite distinct. Most E2 enzymes have a highly conserved Asn residue, like Ubc9 Asn85, which functions as an oxyanion hole that stabilizes the transition state during conjugation (Wu et al., 2003). However, Atg10 homologs do not have an Asn residue equivalent to Ubc9 Asn85. KmAtg10 Asn114 is conserved as Asn/His among Atg10 homolog, suggesting that these Asn/His residues might function as an oxyanion hole in addition to the role of orienting the acceptor lysine. Further structural and biochemical studies are required for characterizing the oxyanion hole of Atg10.

The k_{cat} value for AtAtg12b-KmAtg5 conjugation catalyzed by KmAtg10 (0.045 s^{-1}) was much lower than that for SUMO-RanGAP1 conjugation mediated by Ubc9 (0.66 s^{-1}) but was comparable with those for some other E2-mediated conjugation reactions, such as Ubc9-mediated SUMO-p53 conjugation (0.021 s^{-1}) and RAD6-mediated Ub-histone H2A conjugation (0.032 s^{-1}) (Figure 4G) (Haas et al., 1991; Yunus and Lima, 2006). The abundance of Atg5 was estimated to be 606 molecules per cell, which was considerably small compared with most other proteins (Ghaemmaghami et al., 2003). So, it may not be necessary for Atg10 to possess a higher E2 activity, although we cannot exclude the possibilities that some unknown factor(s) might enhance the E2 activity of Atg10 in vivo. Although the K_d value of the KmAtg10-KmAtg5 interaction was significantly large (~1.5 mM), the apparent K_m value of the AtAtg12b-KmAtg5 conjugation reaction was small enough for an E2-mediated reaction (~10 μM), which appeared to be accomplished through the direct interaction of KmAtg5 with both KmAtg10 and AtAtg12b (Figure 4H). Thus, Atg10 recognizes its substrate Atg5 using both its characteristic accessories (β5, β6) and the thioester-linked modifier molecule (Atg12) and accomplishes the conjugation reaction without E3. Characterization of Atg12-Atg5 interaction will give us further insights into the reaction mechanism.

Another autophagy-related E2, Atg3, also possesses two β strands that are topologically equivalent to β5 and β6 of Atg10 (Figures S1C–S1E) (Yamada et al., 2007). Moreover, it was also reported that Atg3~Atg8 thioester intermediate has higher affinity against PE-containing liposomes than free Atg3 (Oh-oka et al., 2008). So, it is interesting to determine whether Atg3 also utilizes these β strands and the modifier, Atg8, in recognizing its sole target, PE. Atg3 has catalytic-site residues similar to Atg10; Atg3 conserves Tyr and His residues in the positions equivalent to KmAtg10 Tyr56 and Asn114, respectively, and does not conserve a residue equivalent to Ubc9 Asn85. Further structural and biochemical studies on autophagy-related E2s, Atg10 and Atg3 will contribute to the elucidation of both specific and general mechanisms of E2 family enzymes and uncover how these unique E2s regulate autophagy.

EXPERIMENTAL PROCEDURES

Protein Expression and Purification

Plasmid construction, expression, and purification of AtAtg12b were performed as described previously (Suzuki et al., 2005). The KmAtg10 and KmAtg5 genes were amplified by PCR and cloned into either pGEX6P-1 (GE Healthcare, Waukesha, WI, USA) or pPROEX-HTb (Invitrogen, Carlsbad, CA, USA). The KmAtg7 gene was amplified by PCR and cloned into pGBHPS (Kobashigawa et al., 2009). Mutations leading to specific amino acid substitutions were introduced by PCR-mediated site-directed mutagenesis. All constructs were sequenced to confirm their identities and were expressed in *Escherichia coli* BL21 (DE3).

Cells were lysed and glutathione S-transferase (GST)-fused Atg proteins were purified by affinity chromatography using a glutathione-Sepharose 4B column (GE Healthcare). GB1-His-KmAtg7 and His-KmAtg5 were purified by affinity chromatography using a Ni-NTA column (Qiagen, Venlo, the Netherlands). GST and GB1-His were excised from KmAtg10, KmAtg5, and KmAtg7, respectively, with a PreScission protease. (GE Healthcare). KmAtg10 and KmAtg5 were further purified with a glutathione-Sepharose 4B column to remove GST followed by a Superdex75 gel filtration column. His-KmAtg10 and His-KmAtg5 was further purified by a Superdex75 gel filtration column. KmAtg7 was further purified with a Ni-NTA column to remove GB1-His followed by a Superdex 200 gel filtration column. For in vitro pulldown assay, GST-KmAtg5 was further purified by a Superdex200 gel filtration column. For NMR spectrometry, ^{15}N-labeled and ^{13}C- ^{15}N-double-labeled proteins were prepared by growing *E. coli* in M9 media using $^{15}NH_4Cl$ and ^{13}C-glucose as the sole nitrogen and carbon sources, respectively. ^{2}H- ^{15}N-double-labeled proteins for the transferred cross-saturation experiment were prepared by growing *E. coli* in 99.8% D_2O M9 media using $^{15}NH_4Cl$ and 97% $^{2}H_6$-glucose as the sole nitrogen and carbon sources.

Crystallization and Data Collection

A crystal of KmAtg5 was obtained at 293 K by sitting drop vapor diffusion against a well solution of 1.5–1.8 M $(NH_4)_2SO_4$, 1%–4% PEG400, 0.1 M HEPES (pH 6.8) and 10–15 mg/ml KmAtg5. The crystal was cryoprotected through the addition of 15% glycerol (v/v), then flash-cooled, and kept in a stream of nitrogen gas at 100 K during data collection. Diffraction data were collected at SPring8 BL41XU beamline at the wavelength of 1.000 Å and then processed with the HKL2000 program suite (Otwinowski and Minor, 1997). Refinement and data statistics are provided in Table 2. Molecular replacement was performed using the programs BALBES (Long et al., 2008) and MOLREP (Vagin and Teplyakov, 1997) in the CCP4 software suite (Winn et al., 2011). The crystal structure of *S. cerevisiae* Atg5 complexed with the N-terminal region of Atg16 (Protein Data Bank code 2DYO) was used as a search model. Manual building and modification was performed with the molecular modeling program COOT (Emsley et al., 2010), followed by iterative rounds of refinement using the CNS program (Brünger et al., 1998). There are no residues that lie in disallowed regions in a Ramachandran analysis.

NMR Spectroscopy

NMR experiments were carried out at 298 K on a Varian UNITY INOVA 600 spectrometer. Sample of 0.5 mM ^{13}C, ^{15}N-labeled KmAtg10 dissolved in 50 mM phosphate buffer (pH 6.8), 100 mM NaCl, and 5 mM dithiothreitol was prepared and ^{1}H, ^{13}C, ^{15}N resonance assignments of KmAtg10 were performed using the following sets of spectra: [^{1}H- ^{15}N] HSQC, HNCO, HN(CO)CA, HNCA, HN(CA)HA, HBHA(CO)NH, [^{1}H- ^{13}C] HSQC, C(CO)NH, CCH-TOCSY, HCCH-TOCSY, HbCbCgCdHd, and HbCbCgCdCeHe. Spectra were processed by NMRpipe (Delaglio et al., 1995), and data analysis was conducted using the Sparky program (Kneller and Goddard, 1997). Interproton distance restraints for structural calculations were obtained from ^{13}C-edited NOESY-HSQC and ^{15}C-edited NOESY-HSQC spectra using a 75 ms mixing time.

The structure was calculated using the CYANA 2.1 software package (Herrmann et al., 2002). As an input for the final calculation of the three-dimensional structure of KmAtg10, 3282 distance and 225 dihedral angle restraints predicted by TALOS program (Cornilescu et al., 1999) were used. At each stage, 100 structures were calculated using 30,000 steps of simulated annealing, and a final ensemble of 20 structures was selected based on CYANA target function values. The sample solution of the 0.2 mM ^{15}N-labeled KmAtg10 complexed with a 1.25 molar equivalent of nonlabeled KmAtg5 dissolved in 20 mM phosphate buffer (pH 6.8) and 100 mM NaCl was prepared for chemical shift perturbation. Chemical shift perturbations (Δppm) were calculated using the following equation: $\Delta ppm = [(\Delta\delta HN)^2 + (\Delta\delta N/5)^2]^{1/2}$, where ΔδHN and ΔδN are the differences in chemical shift between the free and complex states along the ^{1}H and ^{15}N axes, respectively.

The transferred cross-saturation experiment was carried out using the pulse scheme (Takahashi et al., 2000) at 293 K on a Varian UNITY INOVA 800 spectrometer. Sample of 0.80 mM ^{2}H, ^{15}N-labeled KmAtg10 in complex with 0.5 equivalent of the nonlabeled KmAtg5 was dissolved in 50 mM phosphate buffer (pH 6.8), 100 mM NaCl, and 5 mM ^{2}H-labeled dithiothreitol containing 10% H_2O/90% D_2O. Saturation of the aliphatic protons of KmAtg5 was made using the WURST-2 decoupling scheme (Kupce and Wagner, 1995). The saturation frequency was set at 0 ppm, and the maximum radio-frequency amplitude was 0.26 kHz for WURST-2. The measurement time was 14 hr, with a relaxation delay of 1.0 s and a saturation time of 2.0 s. To evaluate the effect of the residual aliphatic protons within KmAtg10, a transferred cross-saturation experiment without KmAtg5 was also performed under the same conditions. Spectra were processed by NMRpipe (Delaglio et al., 1995), and data analysis was performed using the Sparky program (Kneller and Goddard, 1997). The intensity ratio was calculated as sat (+) / sat (-).

In Vitro Conjugation Assays

In vitro conjugation assays were performed as previously described (Fujioka et al., 2008; Yunus and Lima, 2006, 2009). For KmAtg10∼AtAtg12b thioester intermediate formation under multiturnover conditions, 10 μM KmAtg7, 10 μM KmAtg10, and 10 μM AtAtg12b were incubated in the reaction buffer containing 20 mM Tris-HCl (pH 8.0), 150 mM NaCl, 1 mM ATP, 1 mM $MgCl_2$, and 0.2 mM dithiothreitol at 303 K for 15 min. For KmAtg10∼AtAtg12b thioester intermediate formation under single-turnover conditions, the KmAtg7∼AtAtg12b intermediate was generated by incubating 10 μM KmAtg7 and 10 μM AtAtg12b at 310 K for 20 min in the reaction buffer as mentioned above, then the reaction mixture was diluted 50-fold in buffer containing 50 mM Tris-HCl (pH 8.0), 100 mM NaCl, 50 mM EDTA, 0.2 mM dithiothreitol, and 20 μM KmAtg10 and incubated at room temperature for 15 min. The reaction was stopped by mixing with SDS-PAGE sample buffer. Nu-PAGE 4%–12% Bis-Tris gels (Invitrogen) were used for detecting the KmAtg10∼AtAtg12b thioester intermediate.

For AtAtg12b–KmAtg5 conjugate formation under multiturnover conditions, 10 μM KmAtg7, 10 μM KmAtg10, 10 μM KmAtg5, and 10 μM AtAtg12b were incubated in the reaction buffer as mentioned above at 303 K for 2 hr. The reaction was stopped by mixing with SDS-PAGE sample buffer and proteins were detected by CBB staining. Single-turnover assays for wild-type KmAtg10 and KmAtg10 mutants were carried out as described below. The KmAtg10∼AtAtg12b intermediate was generated by incubating 1 μM KmAtg7, 10 μM KmAtg10 mutants, and 7.5 μM AtAtg12b at 310 K for 20 min in the reaction buffer as mentioned above. The reaction mixture was then diluted 10-fold in buffer containing 50 mM Tris-HCl (pH 8.0), 100 mM NaCl, 50 mM EDTA, 0.2 mM dithiothreitol, and His-KmAtg5 at various concentrations ranging from 0.5–80 μM and incubated at room temperature for 20 s to 20 min. Protein bands were detected using anti-AtAtg12b antibodies. All data based on chemiluminescence were measured within the linear range of the detection method. The images were obtained by Fujifilm LAS4000 imager and quantified using ImageJ software (Abramoff et al., 2004). Initial reaction velocities were calculated at various KmAtg5 concentrations, where the data points were in the linear range. Rates at the 20 and 50 μM wild-type KmAtg5 were estimated with a single time point at 20 s because rates deviated from linearity at later time points. Apparent K_m and k_{cat} for AtAtg12b-KmAtg5 conjugation were determined from nonlinear regression analysis by fitting the data to Michaelis-Menten equation using GraphPad Prism software version 5.03 for Windows (GraphPad Software, La Jolla, CA, USA).

For in vitro pulldown assay, after 10 μM GST-KmAtg5 or GST was incubated with glutathione-Sepharose 4B beads at room temperature, 10 μM His-KmAtg10 (Figure S2A) or 10 μM AtAtg12b with/without His-KmAtg10 (Figure 4H) were loaded to the beads and they were further incubated at room temperature. Washing beads with PBS three times, proteins were eluted with buffer containing 10 mM glutathione and 50 mM Tris-HCl (pH 8.0). The eluates were subjected to Nu-PAGE followed by western blotting using anti-6xHis or anti-AtAtg12b antibodies.

Structural Comparison among E2-like Proteins

The structural comparisons between the solution structure of KmAtg10 and other E2 enzymes, Atg3 (2DYT) and Ubc9 (1U9A), were performed using the DALI search engine. All images are drawn by PyMOL (DeLano, 2002). The catalytic structures of KmAtg10, Atg3, and Ubc9-RanGAP1 were overlaid by minimizing the root-mean-square difference of the Cα atom of KmAtg10 Tyr56, Asn114, and Cys116 with that of the equivalent residue (Tyr87, Asp127, and Cys93 of Ubc9) using the CNS program.

In Vivo Analyses

Yeast *atg10*Δ (10Δ, ScUniv-12) cells were transformed with the pRS316 centromeric vector (vec), the pRS426 multicopy vector (2μ, vec), or indicated plasmids to express wild-type or mutant forms of ScAtg10-2xHA, respectively. Cells were grown in SD/CA(-Ura) medium (Growing), and total cell lysates were prepared and subjected to immunoblotting with anti-HA (3F10, Roche, Indianapolis, IN, USA), anti-Atg12, anti-Atg8, and anti-Ape1 antibodies, respectively.

Crosslinking Experiments

Samples containing 10 μM KmAtg10 and 10 μM KmAtg5 were incubated with or without 100 μM $BM(PEG)_2$ (Thermo Fisher Scientific, Rockford, IL, USA) in buffer containing 50 mM HEPES (pH 7.0), 100 mM NaCl, 10 μM DTNB, and 5 mM EDTA at room temperature for 1 hr. The reaction was quenched by adding 10 mM dithiothreitol to remove the excess nonreacted reagent and incubated at room temperature for 15 min. The reaction was stopped by mixing with nonreducing SDS-PAGE sample buffer and the samples were subjected to SDS-PAGE followed by CBB staining.

SUPPLEMENTAL INFORMATION

Supplemental Information includes four figures and can be found with this article online at doi:10.1016/j.str.2012.04.018.

ACKNOWLEDGMENTS

We are grateful to Dr. H. Nakatogawa for valuable comments on the paper. The synchrotron radiation experiments were performed at the beamline BL41XU at SPring8, Japan. This work was supported by Grants-in-Aid for Young Scientists (A) and Targeted Proteins Research Program from the Ministry of Education, Culture, Sports, Science, and Technology of Japan.

Received: January 20, 2012
Revised: April 24, 2012
Accepted: April 25, 2012
Published online: June 7, 2012

REFERENCES

Abramoff, M.D., Magalhaes, P.J., and Ram, S.J. (2004). Image processing with ImageJ. Biophotonics International *11*, 36–42.

Brünger, A.T., Adams, P.D., Clore, G.M., DeLano, W.L., Gros, P., Grosse-Kunstleve, R.W., Jiang, J.S., Kuszewski, J., Nilges, M., Pannu, N.S., et al. (1998). Crystallography & NMR system: A new software suite for macromolecular structure determination. Acta Crystallogr. D Biol. Crystallogr. *54*, 905–921.

Cornilescu, G., Delaglio, F., and Bax, A. (1999). Protein backbone angle restraints from searching a database for chemical shift and sequence homology. J. Biomol. NMR *13*, 289–302.

Delaglio, F., Grzesiek, S., Vuister, G.W., Zhu, G., Pfeifer, J., and Bax, A. (1995). NMRPipe: a multidimensional spectral processing system based on UNIX pipes. J. Biomol. NMR *6*, 277–293.

DeLano, W. (2002). The PyMOL Molecular Graphics System (Palo Alto, CA: DeLano Scientific LLC).

Emsley, P., Lohkamp, B., Scott, W.G., and Cowtan, K. (2010). Features and development of Coot. Acta Crystallogr. D Biol. Crystallogr. *66*, 486–501.

Fujioka, Y., Noda, N.N., Fujii, K., Yoshimoto, K., Ohsumi, Y., and Inagaki, F. (2008). In vitro reconstitution of plant Atg8 and Atg12 conjugation systems essential for autophagy. J. Biol. Chem. *283*, 1921–1928.

Fujita, N., Itoh, T., Omori, H., Fukuda, M., Noda, T., and Yoshimori, T. (2008). The Atg16L complex specifies the site of LC3 lipidation for membrane biogenesis in autophagy. Mol. Biol. Cell *19*, 2092–2100.

Ghaemmaghami, S., Huh, W.K., Bower, K., Howson, R.W., Belle, A., Dephoure, N., O'Shea, E.K., and Weissman, J.S. (2003). Global analysis of protein expression in yeast. Nature *425*, 737–741.

Haas, A.L., Reback, P.B., and Chau, V. (1991). Ubiquitin conjugation by the yeast RAD6 and CDC34 gene products. Comparison to their putative rabbit homologs, E2(20K) AND E2(32K). J. Biol. Chem. *266*, 5104–5112.

Hanada, T., Noda, N.N., Satomi, Y., Ichimura, Y., Fujioka, Y., Takao, T., Inagaki, F., and Ohsumi, Y. (2007). The Atg12-Atg5 conjugate has a novel E3-like activity for protein lipidation in autophagy. J. Biol. Chem. *282*, 37298–37302.

Herrmann, T., Güntert, P., and Wüthrich, K. (2002). Protein NMR structure determination with automated NOE assignment using the new software CANDID and the torsion angle dynamics algorithm DYANA. J. Mol. Biol. *319*, 209–227.

Hershko, A., and Ciechanover, A. (1998). The ubiquitin system. Annu. Rev. Biochem. *67*, 425–479.

Ichimura, Y., Kirisako, T., Takao, T., Satomi, Y., Shimonishi, Y., Ishihara, N., Mizushima, N., Tanida, I., Kominami, E., Ohsumi, M., et al. (2000). A ubiquitin-like system mediates protein lipidation. Nature *408*, 488–492.

Klionsky, D.J., and Ohsumi, Y. (1999). Vacuolar import of proteins and organelles from the cytoplasm. Annu. Rev. Cell Dev. Biol. *15*, 1–32.

Kneller, D.G., and Goddard, T.D. (1997). SPARKY 3 (San Francisco, CA: University of California).

Kobashigawa, Y., Kumeta, H., Ogura, K., and Inagaki, F. (2009). Attachment of an NMR-invisible solubility enhancement tag using a sortase-mediated protein ligation method. J. Biomol. NMR *43*, 145–150.

Kupce, E., and Wagner, G. (1995). Wideband homonuclear decoupling in protein spectra. J. Magn. Reson. Ser. B *109*, 329–333.

Long, F., Vagin, A.A., Young, P., and Murshudov, G.N. (2008). BALBES: a molecular-replacement pipeline. Acta Crystallogr. D Biol. Crystallogr. *64*, 125–132.

Matsushita, M., Suzuki, N.N., Obara, K., Fujioka, Y., Ohsumi, Y., and Inagaki, F. (2007). Structure of Atg5.Atg16, a complex essential for autophagy. J. Biol. Chem. *282*, 6763–6772.

Mizushima, N. (2007). Autophagy: process and function. Genes Dev. *21*, 2861–2873.

Mizushima, N., Noda, T., Yoshimori, T., Tanaka, Y., Ishii, T., George, M.D., Klionsky, D.J., Ohsumi, M., and Ohsumi, Y. (1998). A protein conjugation system essential for autophagy. Nature *395*, 395–398.

Mizushima, N., Noda, T., and Ohsumi, Y. (1999). Apg16p is required for the function of the Apg12p-Apg5p conjugate in the yeast autophagy pathway. EMBO J. *18*, 3888–3896.

Mizushima, N., Yoshimori, T., and Ohsumi, Y. (2011). The role of Atg proteins in autophagosome formation. Annu. Rev. Cell Dev. Biol. *27*, 107–132.

Nakanishi, T., Miyazawa, M., Sakakura, M., Terasawa, H., Takahashi, H., and Shimada, I. (2002). Determination of the interface of a large protein complex by transferred cross-saturation measurements. J. Mol. Biol. *318*, 245–249.

Nakatogawa, H., Suzuki, K., Kamada, Y., and Ohsumi, Y. (2009). Dynamics and diversity in autophagy mechanisms: lessons from yeast. Nat. Rev. Mol. Cell Biol. *10*, 458–467.

Noda, N.N., Kumeta, H., Nakatogawa, H., Satoo, K., Adachi, W., Ishii, J., Fujioka, Y., Ohsumi, Y., and Inagaki, F. (2008). Structural basis of target recognition by Atg8/LC3 during selective autophagy. Genes Cells *13*, 1211–1218.

Noda, N.N., Ohsumi, Y., and Inagaki, F. (2009). ATG systems from the protein structural point of view. Chem. Rev. *109*, 1587–1598.

Noda, N.N., Ohsumi, Y., and Inagaki, F. (2010). Atg8-family interacting motif crucial for selective autophagy. FEBS Lett. *584*, 1379–1385.

Nonklang, S., Abdel-Banat, B.M., Cha-aim, K., Moonjai, N., Hoshida, H., Limtong, S., Yamada, M., and Akada, R. (2008). High-temperature ethanol fermentation and transformation with linear DNA in the thermotolerant yeast Kluyveromyces marxianus DMKU3-1042. Appl. Environ. Microbiol. *74*, 7514–7521.

Oh-oka, K., Nakatogawa, H., and Ohsumi, Y. (2008). Physiological pH and acidic phospholipids contribute to substrate specificity in lipidation of Atg8. J. Biol. Chem. *283*, 21847–21852.

Ohsumi, Y. (2001). Molecular dissection of autophagy: two ubiquitin-like systems. Nat. Rev. Mol. Cell Biol. *2*, 211–216.

Otwinowski, Z., and Minor, W. (1997). Processing of X-ray diffraction data collected in oscillation mode. In Methods in Enzymology, C.W. Carter and R.M. Sweets, eds. (Charlottesville: University of Virginia), pp. 307–326.

Shintani, T., Mizushima, N., Ogawa, Y., Matsuura, A., Noda, T., and Ohsumi, Y. (1999). Apg10p, a novel protein-conjugating enzyme essential for autophagy in yeast. EMBO J. *18*, 5234–5241.

Suzuki, K., Kirisako, T., Kamada, Y., Mizushima, N., Noda, T., and Ohsumi, Y. (2001). The pre-autophagosomal structure organized by concerted functions of APG genes is essential for autophagosome formation. EMBO J. *20*, 5971–5981.

Suzuki, N.N., Yoshimoto, K., Fujioka, Y., Ohsumi, Y., and Inagaki, F. (2005). The crystal structure of plant ATG12 and its biological implication in autophagy. Autophagy *1*, 119–126.

Takahashi, H., Nakanishi, T., Kami, K., Arata, Y., and Shimada, I. (2000). A novel NMR method for determining the interfaces of large protein-protein complexes. Nat. Struct. Biol. *7*, 220–223.

Tanida, I., Mizushima, N., Kiyooka, M., Ohsumi, M., Ueno, T., Ohsumi, Y., and Kominami, E. (1999). Apg7p/Cvt2p: A novel protein-activating enzyme essential for autophagy. Mol. Biol. Cell *10*, 1367–1379.

Vagin, A., and Teplyakov, A. (1997). MOLREP: an automated program for molecular replacement. J. Appl. Cryst. *30*, 1022–1025.

Wenzel, D.M., Stoll, K.E., and Klevit, R.E. (2011). E2s: structurally economical and functionally replete. Biochem. J. *433*, 31–42.

Winn, M.D., Ballard, C.C., Cowtan, K.D., Dodson, E.J., Emsley, P., Evans, P.R., Keegan, R.M., Krissinel, E.B., Leslie, A.G., McCoy, A., et al. (2011). Overview of the CCP4 suite and current developments. Acta Crystallogr. D Biol. Crystallogr. *67*, 235–242.

Wu, P.Y., Hanlon, M., Eddins, M., Tsui, C., Rogers, R.S., Jensen, J.P., Matunis, M.J., Weissman, A.M., Wolberger, C., and Pickart, C.M. (2003). A conserved catalytic residue in the ubiquitin-conjugating enzyme family. EMBO J. *22*, 5241–5250.

Yamada, Y., Suzuki, N.N., Hanada, T., Ichimura, Y., Kumeta, H., Fujioka, Y., Ohsumi, Y., and Inagaki, F. (2007). The crystal structure of Atg3, an autophagy-related ubiquitin carrier protein (E2) enzyme that mediates Atg8 lipidation. J. Biol. Chem. *282*, 8036–8043.

Yamaguchi, M., Noda, N.N., Nakatogawa, H., Kumeta, H., Ohsumi, Y., and Inagaki, F. (2010). Autophagy-related protein 8 (Atg8) family interacting motif in Atg3 mediates the Atg3-Atg8 interaction and is crucial for the cytoplasm-to-vacuole targeting pathway. J. Biol. Chem. *285*, 29599–29607.

Yamaguti, M., Suzuki, N.N., Fujioka, Y., Ohsumi, Y., and Inagaki, F. (2007). Crystallization and preliminary X-ray analysis of Atg10. Acta Crystallogr. Sect. F Struct. Biol. Cryst. Commun. *63*, 443–445.

Yunus, A.A., and Lima, C.D. (2006). Lysine activation and functional analysis of E2-mediated conjugation in the SUMO pathway. Nat. Struct. Mol. Biol. *13*, 491–499.

Yunus, A.A., and Lima, C.D. (2009). Purification of SUMO conjugating enzymes and kinetic analysis of substrate conjugation. Methods Mol. Biol. *497*, 167–186.

